



Physical Conditions and Kinematics of the Filamentary Structure in Orion Molecular Cloud 1

Yu-Hsuan Teng^{1,2,3} and Naomi Hirano¹

¹ Institute of Astronomy and Astrophysics, Academia Sinica, 11F of Astronomy–Mathematics Building, National Taiwan University, No.1, Section 4, Roosevelt Road, Taipei 10617, Taiwan; elthateng@gmail.com

² Department of Physics, National Taiwan University, No.1, Sec. 4, Roosevelt Road, Taipei 10617, Taiwan

³ Center for Astrophysics and Space Sciences, Department of Physics, University of California San Diego, 9500 Gilman Drive, La Jolla, CA 92093, USA
Received 2019 August 10; revised 2020 March 2; accepted 2020 March 3; published 2020 April 15

Abstract

We have studied the structure and kinematics of the dense molecular gas in the Orion Molecular Cloud 1 (OMC1) region with the N_2H^+ 3–2 line. The $6' \times 9'$ ($\sim 0.7 \times 1.1$ pc) region surrounding the Orion Kleinmann–Low (KL) core has been mapped with the Submillimeter Array (SMA) and the Submillimeter Telescope (SMT). The combined SMA and SMT image, with a resolution of $\sim 5''.4$ (~ 2300 au), reveals multiple filaments with a typical width of 0.02–0.03 pc. On the basis of the non-local thermodynamic equilibrium analysis using the N_2H^+ 3–2 and 1–0 data, the density and temperature of the filaments are estimated to be $\sim 10^7 \text{ cm}^{-3}$ and $\sim 15 \text{ K}$ – 20 K , respectively. The core fragmentation is observed in three massive filaments, one of which shows the oscillations in the velocity and intensity that could be the signature of core-forming gas motions. The gas kinetic temperature is significantly enhanced in the eastern part of OMC1, likely due to the external heating from the high-mass stars in M42 and M43. In addition, the filaments are colder than their surrounding regions, suggesting shielding from the external heating due to the dense gas in the filaments. The OMC1 region consists of three subregions, i.e., north, west, and south of Orion KL, having different radial velocities with sharp velocity transitions. There is a north-to-south velocity gradient from the western to the southern regions. The observed velocity pattern suggests that dense gas in OMC1 is collapsing globally toward the high-mass star-forming region, Orion Nebula Cluster.

Unified Astronomy Thesaurus concepts: [Molecular clouds \(1072\)](#); [Interstellar filaments \(842\)](#); [Star formation \(1569\)](#)

1. Introduction

Filamentary structures have been commonly observed in star-forming clouds at parsec to subparsec scales (e.g., Schneider & Elmegreen 1979; André et al. 2014). The prevalence of a filamentary structure indicates its persistence for a large fraction of the lifetime of a star-forming cloud. Therefore, it is believed that such structures play an important role in star formation processes, and provide clues about the evolution of star-forming clouds. In addition, by examining the low-mass star-forming clouds within 300 pc, Myers (2009) found that all young stellar groups are associated with a “hub–filament structure,” where the “hub” is a high column density region harboring young stellar groups, and the “filaments” are elongated structures with a lower column density radiating from the hub. Such structures also exist in some distant regions that form high-mass stars, although their incidence in massive star-forming regions is still unclear (Myers 2009).

The Orion A molecular cloud, a large-scale filament with an integral-like shape, is the nearest high-mass star-forming region at a distance of 414 pc (Menten et al. 2007). The Orion Molecular Cloud 1 (OMC1), residing at the center of Orion A, is the most massive component ($>2200 M_\odot$) and the most active star-forming region in the Orion Molecular Cloud (Bally et al. 1987). Previous Very Large Array observations in NH_3 (Wiseman & Ho 1998) revealed a typical hub–filament structure in OMC1, in which several filaments radiate from the Orion Kleinmann–Low nebula (Orion KL). These filaments appear to be hierarchical: a large-scale filament consists of narrower filaments at a small scale. Recent high-resolution

observation with the Atacama Large Millimeter/submillimeter Array (ALMA) in N_2H^+ $J = 1$ –0 (Hacar et al. 2018) resolved a total of 28 filaments with a FWHM of ~ 0.02 – 0.05 pc in OMC1, and the cores inside these small-scale filaments are possible sites for star formation. Therefore, studying the physical conditions and gas motions in OMC1 is likely the key to understanding the evolution of hub–filament structures and their relation with star formation.

We present our observations toward the OMC1 region in N_2H^+ 3–2 with an angular resolution of $\sim 5''.4$ obtained using the Submillimeter Array (SMA) and the Submillimeter Telescope (SMT). Further analyses using the N_2H^+ 1–0 data provided by Hacar et al. (2018) are also presented. The rotational transitions of N_2H^+ are known to be good tracers of dense and quiescent gas. With a critical density of $\sim 10^6 \text{ cm}^{-3}$, which is higher than that of ammonia studied by Wiseman & Ho (1998), N_2H^+ 3–2 can probe the dense gas inside the subparsec scale filaments that are directly related to star formation. In addition, N_2H^+ is less affected by depletion even in dense and cold environments, and is also less affected by dynamic processes such as outflows and expanding H II regions.

This study investigates the structure, physical conditions, and gas motions in the OMC1 region. We describe the details of our observations and data reduction in Section 2, and present the results in Section 3. The structural properties, physical conditions, and gas kinematics are analyzed in Section 4. Finally, we discuss the implications of these results in Section 5, and summarize our conclusions in Section 6.

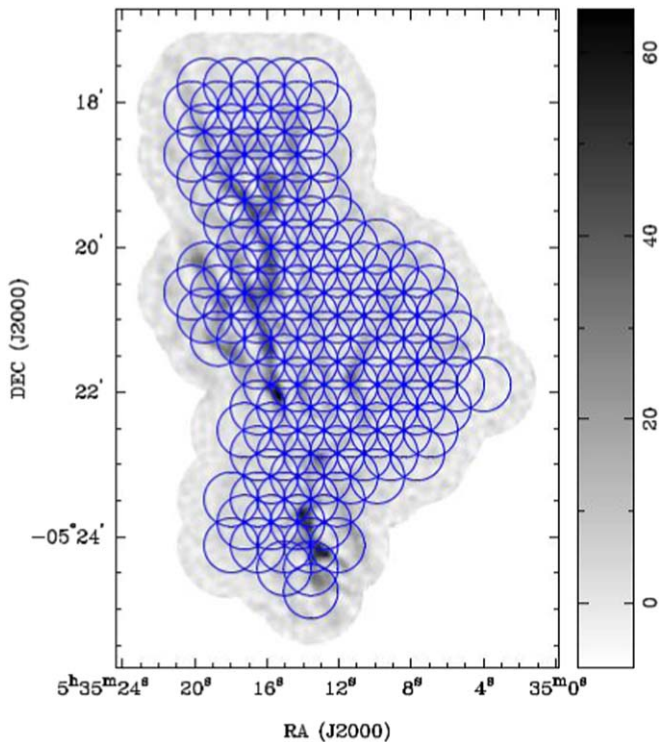


Figure 1. Integrated intensity map made by only the SMA observation. The 144 pointings covering the OMC1 region are overlaid on the SMA map.

2. Observations and Data Reduction

2.1. 1.1 mm Observations with the SMA

Observations of the N_2H^+ $J = 3-2$, HCO^+ $J = 3-2$, and HCN $J = 3-2$ lines together with the 1.1 mm continuum were carried out with the SMA on 2014 February 14, 20, and 24. A subcompact configuration with six antennas in the array was used, providing baselines ranging from 9.476 to 25.295 m. The shortest and longest uv distances are 5.6 k λ and 23.6 k λ , respectively. The primary beam of the 6 m antennas had a size of 42'' in half-power beam width (HPBW), and the synthesized beam size was 5''.53 \times 5''.25. The bandwidth was 4 GHz per sideband, and the frequency resolution was 203 kHz that corresponds to the velocity resolution of ~ 0.22 km s $^{-1}$ at the rest frequency of N_2H^+ 3–2. Using a 144 pointing mosaic with a Nyquist sampled hexagonal pattern, as shown in Figure 1, the observed area covered $\sim 5' \times 7'$. In order to obtain uniform uv coverage for 144 pointings, we observed each pointing for 5 s and visited all pointings in a loop. Each of the 144 pointings was visited three times in each observing run, giving a total on-source integration time per pointing of 45 s.

The visibility data were calibrated using the MIR/IDL software package.⁴ The gain calibrators were 0501-019 and 0607-085, the flux calibrator was Ganymede on February 14 and Callisto on the other two days, and the bandpass calibrator was 3C279. The image processing was carried out using the MIRIAD package (Sault et al. 1995). The image cube was generated with Briggs weighting with a robust parameter of 0.5, followed by a nonlinear joint deconvolution using the CLEAN-based algorithm, MOSSDI. The final data cube has a rms noise level of ~ 0.5 K for a ~ 0.22 km s $^{-1}$ velocity channel. In this paper, we focus on the results and analyses of the N_2H^+

line. Results of HCO^+ and HCN will be presented in a forthcoming paper.

2.2. 1.1 mm Observations with the SMT

We simultaneously observed the N_2H^+ $J = 3-2$ and HCO^+ $J = 3-2$ lines on 2018 November 16 and 17 using the SMT of the Arizona Radio Observatory. We used the SMT 1.3 mm ALMA band 6 receiver and the filter-bank backend. The beam size was 28''.45 in HPBW at the frequency of N_2H^+ 3–2, and the main-beam efficiency is 0.71 ± 0.05 . The on-the-fly mode was used in order to cover the mapping area of $6' \times 9'$ centered at R.A. (J2000) = 5^h35^m12^s.1 and decl. (J2000) = $-5^\circ 21' 15''.4$. The data were reduced with CLASS.⁵ The rms noise levels were ~ 0.3 K at a spectral resolution of 250 kHz (~ 0.27 km s $^{-1}$).

2.3. SMA and SMT Data Combination

We combined the data cubes of the SMA and SMT by using the MIRIAD task *immerge*. The method of this task, known as feathering, linearly merges two images with different resolutions in their Fourier domain (i.e., spatial frequency). In the case of combining the single-dish and mosaicing data, *immerge* gives unit weight to the single-dish data at all spatial frequencies, and tapers the low spatial frequencies of the mosaicing data, so as to produce the Gaussian beam of the combined data equal to that of the mosaicing data. Inputs of *immerge* include the “CLEANed” SMA image cube, SMT image cube, and the flux calibration factor. After checking the consistency in the flux scale of two input image cubes, we set the flux calibration factor to 1. The integrated intensity (moment 0) map and the intensity-weighted radial velocity (moment 1) map after combination are shown in Figure 2. The angular resolution and the rms noise level of the combined map are $\sim 5''.4$ and 1.0 K km s $^{-1}$, respectively.

2.4. N_2H^+ $J = 1-0$ Observations with ALMA and IRAM 30 m

To analyze the physical properties of the filamentary structure in high resolution, we use the N_2H^+ 1–0 data cube provided by Hacar et al. (2018), where the ALMA and IRAM 30 m data were combined (Hacar 2018). The ALMA + IRAM 30 m combined image cube has a circular beam with a size of 4''.5 in FWHM, and a rms level of 25 mJy beam $^{-1}$ at a spectral resolution of 0.1 km s $^{-1}$. The observational details are described in Hacar et al. (2017, 2018).

3. Results

Figure 2 presents the moment 0 (integrated intensity) and moment 1 (intensity-weighted radial velocity) maps of the SMA + SMT combined image. Figure 2(a) shows that most of the emission comes from the filamentary structure with a typical FWHM of 0.02–0.03 pc. Several high-intensity and clumpy structures can also be seen inside the filaments. Orion KL at R.A. (J2000) = 5^h35^m14^s.5 and decl. (J2000) = $-5^\circ 22' 30''$ is near the center of the maps. Differently from observations in a continuum or most other molecular lines, there is no significant N_2H^+ emission from the Orion KL region due to the destruction of N_2H^+ molecules in active regions.

Figure 2(b) reveals that the radial velocity distribution shows a trimodal pattern; the bright filaments to the north of Orion KL

⁴ <https://www.cfa.harvard.edu/rtdc/SMAdata/process/mir/>

⁵ <http://www.iram.fr/IRAMFR/GILDAS>

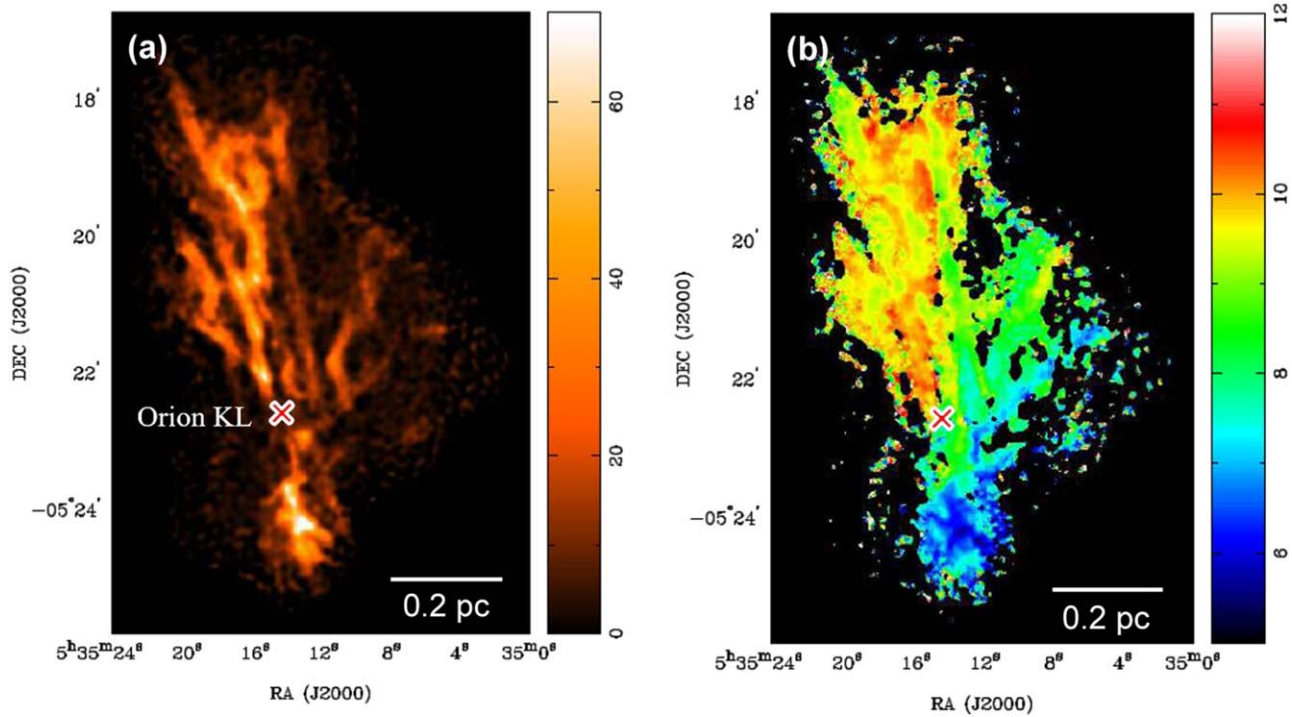


Figure 2. Moment 0 (K km s^{-1}) and moment 1 (km s^{-1}) of the combined SMA and SMT data in N_2H^+ 3–2. The cross depicts the position of Orion KL at (R.A., decl.) = ($5^{\text{h}}35^{\text{m}}14^{\text{s}}.5$, $-5^{\circ}22'30''$).

have a velocity range of $\sim 9\text{--}11 \text{ km s}^{-1}$ (hereafter, referred to as the northern region), the fainter filaments extending to the northwest are seen at $\sim 7\text{--}9 \text{ km s}^{-1}$ (western region), and the ones to the south of Orion KL are at $\sim 5\text{--}7 \text{ km s}^{-1}$ (southern region, also known as OMC1-South). These three regions with different velocities converge at the Orion KL region. The velocity difference between the northern and western regions was also reported by Wiseman & Ho (1998) and Monsch et al. (2018) based on their NH_3 observations. A clearer analysis for the velocity transition among the three regions will be presented in Section 4.2.

In order to derive physical conditions in different subregions, we use the ALMA + IRAM 30 m image in N_2H^+ 1–0 for analyses in Section 4.3. The high-resolution 3–2/1–0 ratio map (Figure 3) was made using the SMA + SMT image and the ALMA + IRAM 30 m image convolved to the same beam size as the SMA + SMT image. Figure 3 reveals that the 3–2/1–0 ratio is higher overall in the eastern part of OMC1. In addition, the 3–2/1–0 ratio tends to be lower in the filament regions as compared to the surrounding nonfilament regions. The typical line ratio in the filament regions is ~ 1.0 , even in the eastern part of OMC1, while that of the nonfilament region is ~ 2.2 . As different ratios may imply different physical conditions, we determine the physical parameters of the filament and nonfilament regions in Section 4.3.

4. Analysis

4.1. Structural Properties of OMC1

4.1.1. Filament Identification

Filament identification is done by applying the python package *FilFinder* (Koch & Rosolowsky 2015) to the SMA + SMT combined moment 0 map. The *FilFinder* algorithm segments filamentary structure by using adaptive thresholding,

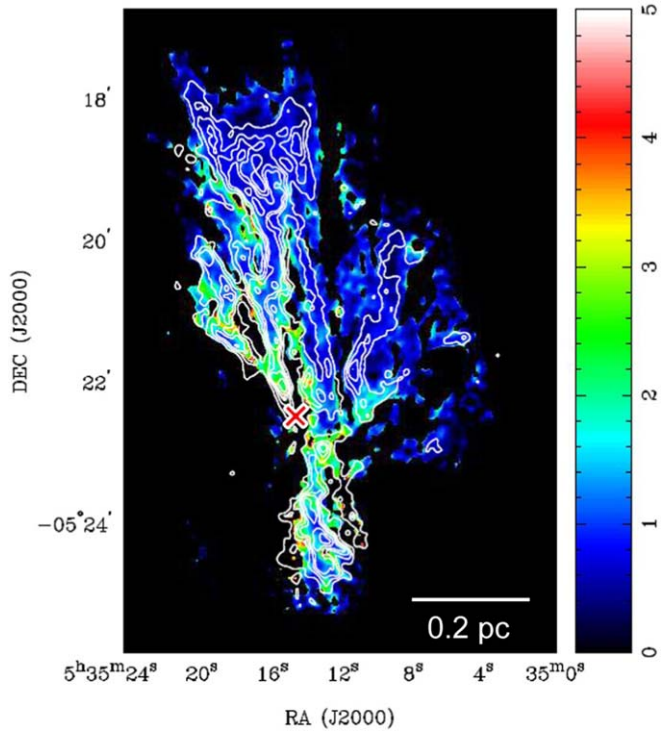


Figure 3. N_2H^+ 3–2/1–0 intensity ratio map using the 1–0 image observed with ALMA + IRAM 30 m (Hacar et al. 2018). Contour levels of N_2H^+ 3–2 moment 0 are overlaid on the line ratio map.

which performs thresholding over local neighborhoods and allows for the extraction of structure over a large dynamic range. Input parameters for *FilFinder* include: (1) global threshold—the minimum intensity for a pixel to be included; (2) adaptive threshold—the expected full width of filaments for

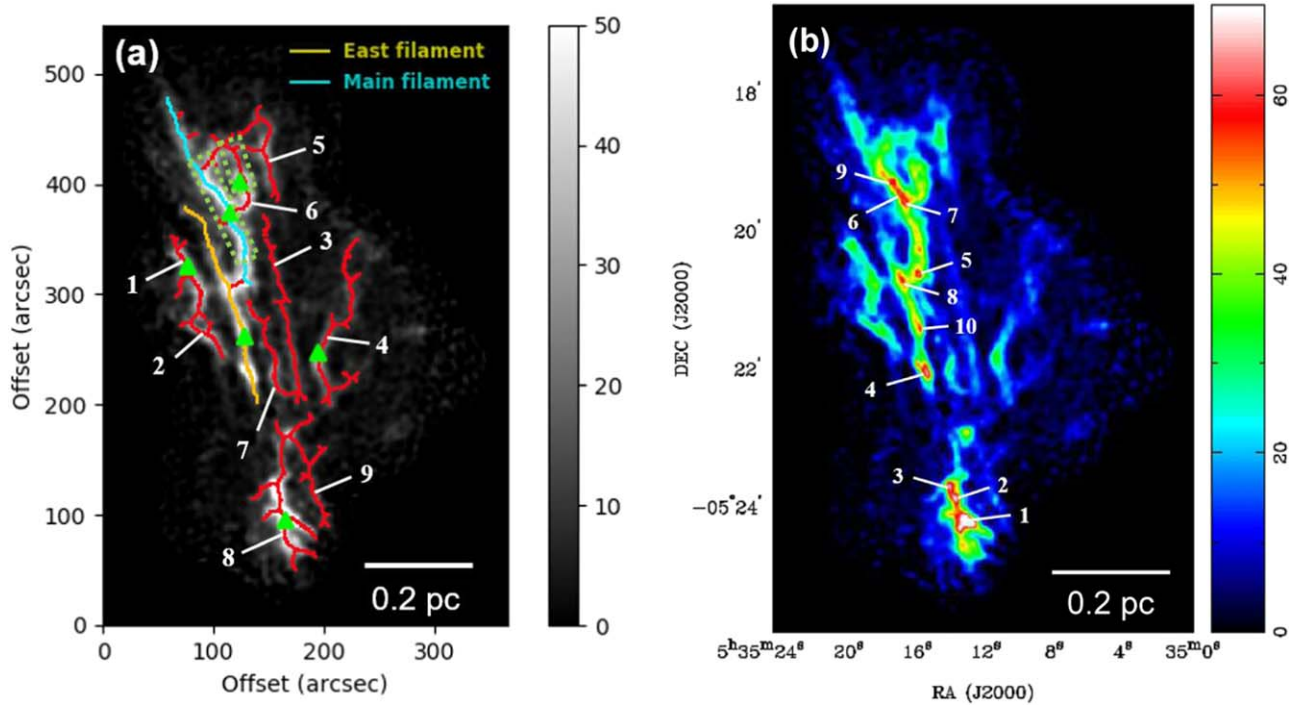


Figure 4. (a) Filaments identified using the *FilFinder*, including the main (blue) and east (yellow) filaments and others (red). The dashed green boxes enclose the regions where multiple velocity components are presented, and the green triangles mark the locations where spectra are shown in Figure 5. (b) Positions of the 10 cores identified using *2-D Clumpfind*.

Table 1
Properties of the Identified Filaments

Filament	Length (± 0.001 pc)	Width _{FWHM} (± 0.001 pc)	M_{lin} ($M_{\odot} \text{pc}^{-1}$)	Δv (km s^{-1})	$\Delta v_{\text{nt}}/c_s(T)$	M_{crit} ($M_{\odot} \text{pc}^{-1}$)	$M_{\text{lin}}/M_{\text{crit}}$
Main	0.349	0.025	94.2–101.7	1.0 ± 0.2	1.5	119.7	0.79–0.85
East	0.365	0.023	78.5–85.6	0.9 ± 0.3	1.3	103.8	0.76–0.83
1	0.159	0.024	84.0	0.6 ± 0.2	0.85	66.0	1.27
2	0.100	0.023	76.2	0.7 ± 0.3	1.0	76.9	0.99
3	0.279	0.017	42.5	1.3 ± 0.6	1.9	177.6	0.24
4	0.303	0.020	61.8	1.1 ± 0.3	1.6	137.3	0.45
5	0.155	0.024	84.0	1.0 ± 0.5	1.5	119.7	0.70
6	0.124	0.033	166.3	1.1 ± 0.3	1.6	137.3	1.21
7	0.175	0.022	68.9	1.0 ± 0.4	1.5	119.7	0.58
8	0.237	0.022	81.5–121.0	2.0 ± 0.9	2.95	371.6	0.22–0.33
9	0.159	0.017	42.5	1.0 ± 0.3	1.5	119.7	0.36

adaptive thresholding; (3) smooth size—scale size for removing small noise variations; (4) size threshold—minimum number of pixels for a region to be considered as a filament.

We set 9 K km s^{-1} as the global threshold. To focus on filaments with lengths $\gtrsim 0.1$ pc, we set the size threshold as 400 square pixels, where the pixel size is 1 arcsec^2 . The adaptive threshold is set to 0.06 pc, which is approximately twice the width of the filaments, and the smooth size is set to 0.03 pc. We find the result matches better with identification by human eyes when the smooth size is set to ~ 0.5 times the adaptive threshold. The smaller we set the smooth size, the more short branches would be identified. On the other hand, a larger smooth size tends to make filaments connected, since a larger region of data is smoothed.

In total, 11 filaments have been identified. Figure 4(a) shows the result of filament identification, where the gray-scale image is the combined moment 0 map, and the colored lines are the identified major axes for each filament. The identified filaments

and their lengths and widths are listed in Table 1, together with the physical properties described in Section 5.1. Since the hyperfine components in N_2H^+ 3–2 cannot be separated, the identification is based on the moment 0 map instead of the 3D data cube. We have estimated the typical FWHM of the identified filaments by fitting a Gaussian to the several cuts perpendicular to the filaments. The FWHM of these filaments are 0.02 – 0.03 pc, which is consistent with those identified in Hacar et al. (2018) based on the ALMA + IRAM 30 m observations in N_2H^+ 1–0.

Hacar et al. (2018) has identified the filaments in Orion A with a different algorithm based on the 3D data cube. Since we identified the filaments in 2D using the moment 0 map, the results are different from those of 3D if there are multiple velocity components in the same line of sight. For example, our main filament and filament 6, which can be clearly seen in the moment 0 map, are not identified by Hacar et al. (2018). As shown in Figure 5(a) and (b), these two filaments contain

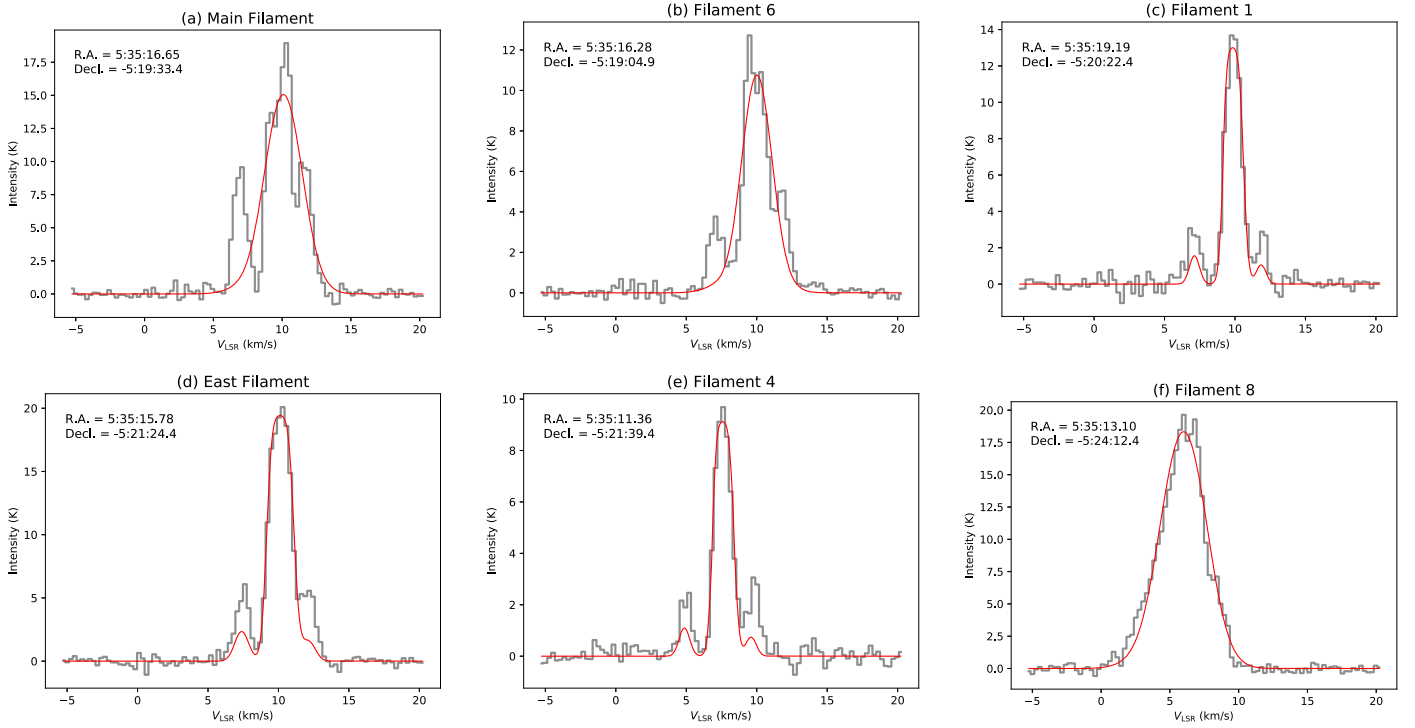


Figure 5. Spectra of the six representative positions of the filaments marked in Figure 4(a). Each spectrum (gray histogram) was obtained by averaging the $5'' \times 5''$ area. Red curves are the results of the hyperfine spectral fitting using the single-velocity component. Part of the (a) main filament and (b) filament 6 have multiple velocity components along the line of sight. (c)–(f) Other filaments in OMC1 have single-component spectra. The deviation between the observed and fitted satellite components in (c)–(e) suggests a non-LTE physical condition (see Section 4.2).

multiple velocity components along the line of sight, which could cause a difference between the results of 2D- and 3D-based algorithms. Apart from these filaments, other OMC1 filaments show a single-velocity component in the spectra. Therefore, there is no significant difference in the results between 2D and 3D identifications.

The moment 0 images in N_2H^+ reveal three filaments with high-intensity clumpy cores, one of which is in the OMC1-South filament 8. We will refer to the two prominent filaments in the northern region as the *main filament* and the *east filament*, which are shown in blue and yellow, respectively, in Figure 4(a). The gas kinematics inside these filaments will be analyzed in Section 4.4.

4.1.2. Core Identification

We identify the high-intensity cores inside the filaments by using the 2D version of *Clumpfind* (Williams et al. 1994). The *Clumpfind* algorithm contours input data with the values assigned by users, and then distinguishes each core region by those values. It starts from the highest contour level, and then works down through the lower levels, finding new cores and extending previously defined ones until the lowest contour level is reached. We use the combined SMA + SMT integrated intensity map as the input data, and set the contour levels as 50, 53.6, 57.2, 60.8, and 64.4 K km s⁻¹. The spacing of the contour levels are set constantly as $\Delta T = 2T_{\text{rms}} = 3.6$, which could lower the percentage of false detection to <2% as suggested in Williams et al. (1994).

Figure 4(b) shows the positions of the 10 cores identified by 2-D *Clumpfind*. Table 2 lists the properties of these cores including position, peak flux, and effective radius (R_{eff}), which are all direct outputs of 2-D *Clumpfind*. Note that the R_{eff} in

Clumpfind is defined as $R_{\text{eff}} = \sqrt{A/\pi}$, where A is the area with emission above the criteria. In Table 2, the line width (Δv) is determined by hyperfine spectral fitting (see Section 4.2), the mass (M_{core}) is derived by using the densities determined from non-local thermodynamic equilibrium (non-LTE) analysis (see Section 4.3), and the virial mass (M_{vir}) is calculated from the line width using Equation (12) (see Section 5.1).

4.2. Hyperfine Spectral Fitting

To determine the physical parameters, we conduct hyperfine spectral fitting on the combined SMA and SMT data for the regions with signal-to-noise ratio > 5. We fit the V_{LSR} , line widths (Δv), excitation temperatures (T_{ex}), and total opacities (τ_{tot}) under the assumption of LTE. With the relative intensities among 16 main hyperfine components for the N_2H^+ 3–2 line (Caselli et al. 2002), the opacity of each component is assumed as a Gaussian profile

$$\tau_i(v) = \tau_i \exp \left[-4 \ln 2 \left(\frac{v - v_i - v_{\text{sys}}}{\Delta v} \right)^2 \right], \quad (1)$$

where v_i is the velocity offset from the reference component and v_{sys} is the systemic velocity. Then, we obtain the optical depths of the multiplets as

$$\tau(v) = \tau_{\text{tot}} \sum_{i=1}^{16} R_i \exp \left[-4 \ln 2 \left(\frac{v - v_i - v_{\text{sys}}}{\Delta v} \right)^2 \right], \quad (2)$$

where R_i is the relative intensity for the i th hyperfine component, and $\tau_i = \tau_{\text{tot}} R_i$. The brightness temperature at each pixel can be represented as

$$T_b(v) = [J(T_{\text{ex}}) - J(T_{\text{bg}})][1 - \exp(-\tau(v))], \quad (3)$$

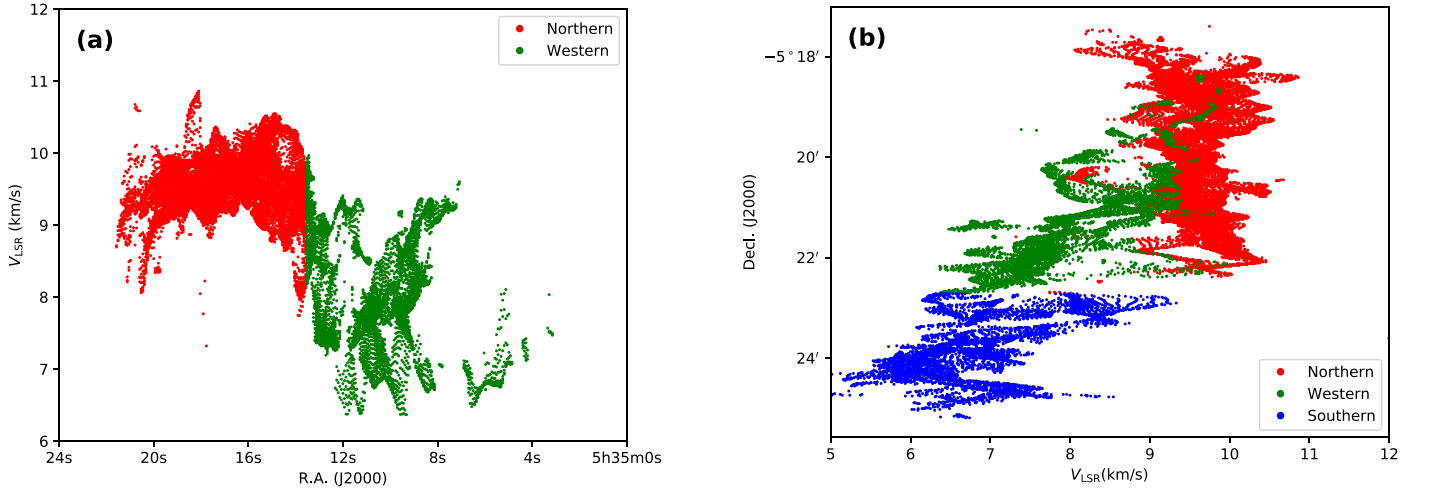


Figure 6. N_2H^+ 3–2 radial velocities of (a) the northern and western regions as a function of R.A., and (b) all three regions as a function of decl.

Table 2
Properties of the Identified Cores

Core	R.A. (J2000.0)	Decl. (J2000.0)	Peak Flux (K km s ⁻¹)	R_{eff} (arcseconds)	Δv (km s ⁻¹)	M_{core} (M_{\odot})	M_{vir} (M_{\odot})
1	05:35:13.10	−5:24:12.4	84.3	8.9	3.5	14.4–45.6	46.1
2	05:35:13.70	−5:23:52.4	69.4	5.6	2.8	3.6–11.3	18.5
3	05:35:14.10	−5:23:41.4	66.5	4.7	1.6	2.0–6.4	5.0
4	05:35:15.37	−5:22:04.4	66.0	5.1	2.0	2.6–8.2	8.5
5	05:35:15.84	−5:20:38.4	63.4	3.5	0.9	0.9–2.8	1.2
6	05:35:16.90	−5:19:27.4	61.9	4.0	...	1.3–4.2	...
7	05:35:16.70	−5:19:34.4	60.8	4.4	...	1.7–5.3	...
8	05:35:16.84	−5:20:42.4	59.2	3.6	2.2	0.9–3.0	7.4
9	05:35:17.37	−5:19:17.4	58.7	4.2	...	1.5–4.7	...
10	05:35:15.77	−5:21:24.4	57.1	2.6	1.1	0.4–1.1	1.3

where T_{bg} is the cosmic background temperature (2.73 K), and

$$J(T) = \frac{\frac{h\nu}{k}}{\exp\left(\frac{h\nu}{kT}\right) - 1}. \quad (4)$$

Figure 5 presents the observed spectra obtained by averaging the $5'' \times 5''$ regions marked in Figure 4(a). The best-fit single-velocity components (in red) are overlaid on the spectra. Note that the multiple velocity components are only limited to the regions near cores 6, 7, and 9 and the northern part of filament 6, as indicated by the dashed green boxes in Figure 4(a). We applied the single-component fitting to the spectra of these regions, because two-component fitting requires too many parameters. Inside the regions with multiple components, the fitted V_{LSR} are still dominated by the major components, although the fitted line widths are highly affected by secondary components.

Using the centroid velocities determined from the hyperfine fitting, we illustrate the velocity distribution along R.A. and decl., respectively. Figure 6(a) shows the radial velocities for all the N_2H^+ 3–2 components fitted in the northern and western regions. The figure reveals a sharp velocity transition near R.A. (J2000) = 5^h35^m14^s, where a clear boundary can also be seen in Figure 2(b) between the northern and western regions. Figure 6(b) shows the radial velocities of all three regions as a function of decl. While the velocities of the northern region are almost constant, those of the western region decrease from

north to south and continuously connected to those of the southern region. Such a velocity decrease from north to south in OMC1 has been reported in Hacar et al. (2017, 2018), and interpreted as the gravitational collapse of OMC1. Figure 6(b) shows that the gas in the western region is accelerated toward OMC1-South.

Comparing the fitting results with the observed spectra, we found that the observed satellite components are much brighter than those predicted by the LTE assumption (e.g., Figure 5(c)–(e)). In addition, when the line is optically thin ($\tau_{\text{tot}} \ll 1$), the fitting cannot constrain T_{ex} and τ_{tot} , because Equation (3) will be reduced to

$$T_b(v) \simeq \tau_{\text{tot}} \cdot T_{\text{ex}}, \quad (5)$$

indicating that the T_{ex} and τ_{tot} can be determined arbitrarily. Therefore, we conduct non-LTE analysis in Section 4.3 to derive the physical conditions.

4.3. N_2H^+ RADEX Non-LTE Modeling

Using RADEX (Van der Tak et al. 2007), a non-LTE radiative transfer code, we construct spectra models in N_2H^+ 3–2 and 1–0. The synthetic spectra are constructed with the equation

$$T_b(v) = \Psi \left(\frac{\sum J(T_{\text{ex}}^i) \tau_i(v)}{\sum \tau_i(v)} - J(T_{\text{bg}}) \right) (1 - e^{-\sum \tau_i(v)}), \quad (6)$$

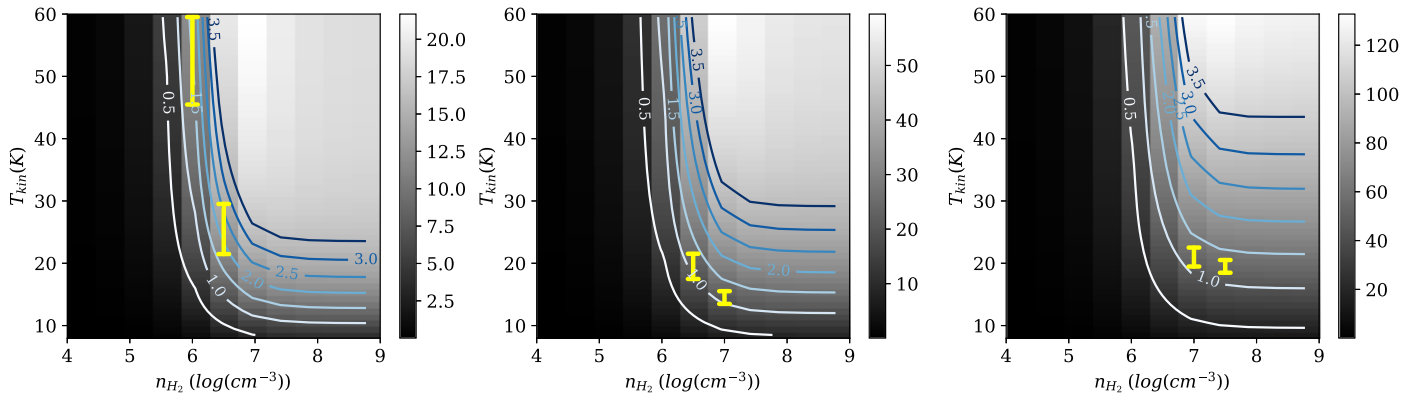


Figure 7. Slices in the non-LTE model grid for $N(\text{N}_2\text{H}^+)/\Delta\nu = 5 \times 10^7, 5 \times 10^{7.5},$ and $5 \times 10^8 \text{ s cm}^{-3}$ from left to right, which corresponds to $N(\text{N}_2\text{H}^+) = 10^{13}, 3 \times 10^{13},$ and 10^{14} cm^{-2} for a region with $\Delta\nu = 2.0 \text{ km s}^{-1}$. The background in gray scale shows the integrated spectra model of N_2H^+ 3–2, and the contour levels indicate the 3–2/1–0 intensity ratio model. The yellow bars from left to right show possible solutions satisfying the conditions of the nonfilament, low-intensity, and core regions, respectively (see Table 3).

where T_{ex}^i and $\tau_i(\nu)$ represent the excitation temperature and optical depth for all hyperfine components in the 3–2 or 1–0 transitions, and Ψ is the beam filling factor. In our models, the beam filling factors are assumed to be unity. We also construct an intensity ratio model by dividing the integrated spectra model in N_2H^+ 3–2 with that in N_2H^+ 1–0.

The constructed models can be represented by a three-dimensional grid, where the three axes are H_2 density (n_{H_2}) ranging from 10^4 – 10^9 cm^{-3} , kinetic temperature (T_{kin}) ranging from 8 K–60 K, and the ratio of N_2H^+ column density to line width ($N(\text{N}_2\text{H}^+)/\Delta\nu$) ranging from 5×10^7 – $5 \times 10^8 \text{ s cm}^{-3}$. The step sizes of the grid are 1 K for T_{kin} and 0.5 in decimal log scale for both $N(\text{N}_2\text{H}^+)$ and n_{H_2} . As $N(\text{N}_2\text{H}^+)/\Delta\nu$ is the input parameter in RADEX, the estimation of $N(\text{N}_2\text{H}^+)$ varies among regions with different line widths. Based on our fitting results, the line width in OMC1 could vary from ~ 1 to 3 km s^{-1} .

Figure 7 presents the constructed non-LTE model, where the gray-scale background shows the integrated spectra model in N_2H^+ 3–2, and the contour levels show the 3–2/1–0 ratio model. By applying the observed integrated intensity and line ratio in this model, physical parameters (n_{H_2} , T_{kin} , and $N(\text{N}_2\text{H}^+)/\Delta\nu$) in different subregions can be constrained. For instance, the two bars on the first panel of Figure 7 indicate the two possible solutions that satisfy the conditions with an intensity of 7 – 15 K km s^{-1} and a line ratio of 2.2 ± 0.4 . The corresponding physical conditions of the left and right bars are $n_{\text{H}_2} = 10^6 \text{ cm}^{-3}$ and $T_{\text{kin}} = 45$ – 60 K , and $n_{\text{H}_2} = 3 \times 10^6 \text{ cm}^{-3}$ and $T_{\text{kin}} = 21$ – 30 K , respectively.

We use our SMA + SMT data in N_2H^+ 3–2 together with the ALMA + IRAM 30 m data in N_2H^+ 1–0 for the non-LTE analysis, where the scale size is $5''.4$ ($\sim 0.01 \text{ pc}$). Based on the 3–2 moment 0 map, we define three regions for analysis. The first region is defined as the core regions with integrated intensity 50 – 60 K km s^{-1} and a 3–2/1–0 ratio of 1 ± 0.3 . The second region is the lower intensity regions inside the filaments (20 – 40 K km s^{-1}) with a similar line ratio of 1 ± 0.3 , and the third region is the nonfilament region with low intensities (7 – 15 K km s^{-1}) and a higher line ratio of 2.2 ± 0.4 . The spectra averaged in these subregions are compared with the model spectra. The derived physical parameters for the non-LTE analysis together with the criteria of the three subregions are listed in Table 3.

Table 3
Parameters for Non-LTE Analysis

	Core Regions ($>50 \text{ K km s}^{-1}$)	Low-intensity Regions	Nonfilament Regions
$n_{\text{H}_2} (\text{cm}^{-3})$	10^7 or 3×10^7	3×10^6 or 10^7	10^6 or 3×10^6
$T_{\text{kin}} (\text{K})$	19–23 or 18–20	17–22 or 13–16	> 45 or 21–30
$N(\text{N}_2\text{H}^+)/\Delta\nu$ (s cm^{-3})	5×10^8	1.5×10^8	5×10^7
Intensity (K km s^{-1})	50–60	20–40	7–15
Typical ratio	1 ± 0.3	1 ± 0.3	2.2 ± 0.4

By comparing between the filament and nonfilament regions, we find that the filament regions have a higher density of $\sim 10^7 \text{ cm}^{-3}$ and a lower temperature of ~ 15 – 20 K than the nonfilament regions. As the major heating sources may come from outside the filaments, it is likely that the dense gas in the filaments could block the outer radiation, leading to a lower temperature in the filaments (see Section 5.2 for further discussion). Inside the filaments, the core regions have a higher N_2H^+ column density than the low-intensity regions, if we assume similar line widths in these regions. Also, the volume density of the core regions are generally higher than the low-intensity regions. On the other hand, there is no significant difference in temperature between the core and the low-intensity regions, although the derived T_{kin} is slightly higher in the core regions.

Using the volume densities determined from the non-LTE analysis and the filament widths, we have estimated the masses of the cores and the line masses of the filaments under the assumption of uniform cylindrical filaments. We adopted this method instead of using the column density of N_2H^+ because the fractional abundance of N_2H^+ is highly uncertain in the regions close to Orion KL and because the inclination of each filament is also uncertain. The density is assumed to be $n_{\text{H}_2} = 3 \times 10^6 \text{ cm}^{-3}$ for the filaments without cores. For those with cores, i.e., main filament, east filament, and filament 8, we use two possible core densities (i.e., 10^7 or $3 \times 10^7 \text{ cm}^{-3}$) determined in this section for the core regions and $n_{\text{H}_2} = 3 \times 10^6 \text{ cm}^{-3}$ for the regions outside the cores. If we adopt the higher density solution, i.e., 10^7 cm^{-3} , for the low-intensity regions of the filaments, the line masses of the

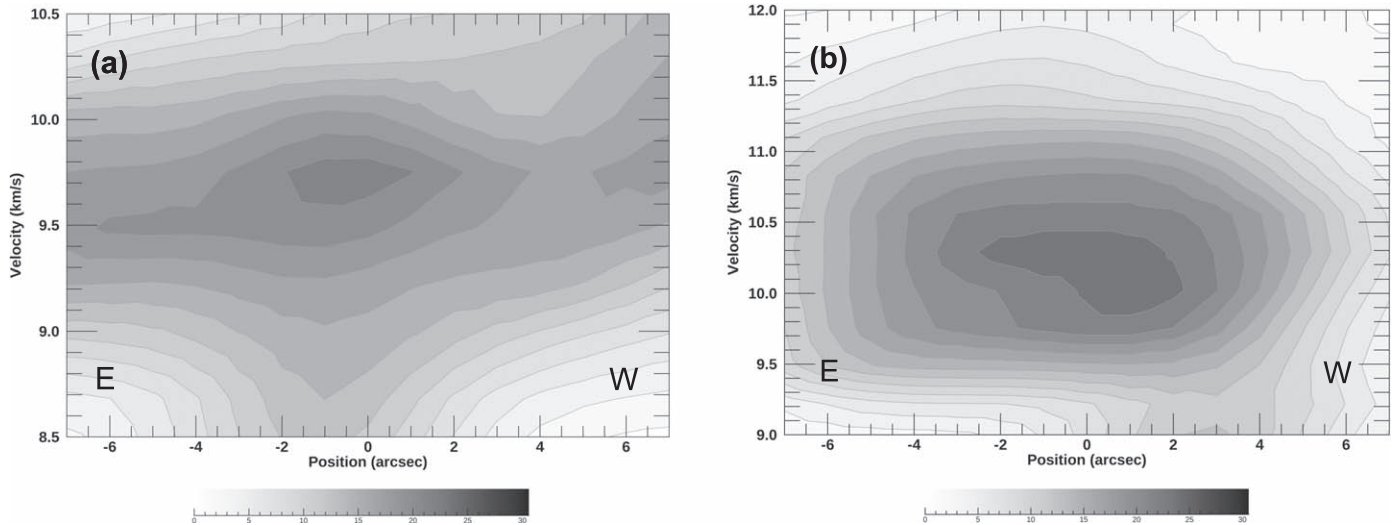


Figure 8. Position-velocity (P-V) diagrams across (a) core 8 and (b) core 4 inside the east filament.

filaments could be higher by a factor of ~ 3 . On the other hand, if we adopt the radial density profile of the isothermal cylinder with the same central density (e.g., Ostriker 1964), the line mass included in the radius of 0.01–0.015 pc (i.e., half of the filament width) becomes lower by a factor of two. Properties of the identified filaments and cores are summarized in Tables 1 and 2, respectively, and will be discussed in Section 5.1.

4.4. Gas Kinematics of the Filaments

Characterizing the gas motion inside the filaments requires the studies of velocity structure. We investigate the radial velocity fields along both the major and minor axes of the filaments in OMC1, and compare our results with existing filament formation model and core formation model. Since the main filament and the east filament are identified with core fragmentation, we focus on the analyses of these two filaments.

4.4.1. Minor-axis Analysis

Systematic velocity gradients perpendicular to the filaments have been observed in the filaments of both low- and high-mass star-forming regions (e.g., Schneider et al. 2010; Beuther et al. 2015; Dhabal et al. 2018). Such velocity gradients across the filaments can be explained by the projection of gas accretion toward the filament axes (Dhabal et al. 2018) or the rotation of filaments (Olmi & Testi 2002). In order to assess whether the OMC1 filaments show similar features, we analyze the velocity fields along the minor axes.

In the main and the east filaments, there is no systematic velocity gradient along the minor axes. However, local velocity gradients of $\sim 0.3 \text{ km s}^{-1}$ are observed in cores 4 and 8 in the east filament. On the other hand, there is no significant velocity gradient in cores 5 and 10. The velocity gradients in cores 6, 7, and 9 in the northern part of the main filament are unclear due to the secondary velocity component along the line of sight. Figure 8 shows P-V diagrams across core 8 and core 4. The directions of velocity gradients across these cores are not consistent; the velocity increases from east to west in core 8, while it decreases in core 4. Such velocity gradients with different directions along the same filament have also been

observed along the massive DR21 filament, although its origin is still unclear (Schneider et al. 2010).

Using the effective radii determined in Section 4.1.2, i.e., $R_{\text{eff}} = 5''.1$ and $3''.6$ for core 4 and core 8, respectively, the velocities at R_{eff} were determined from the spectral fitting. Then, the velocity gradient (∇V) along the east-west direction was estimated using the velocity difference at the core boundaries and the effective diameter. Assuming a linear velocity variation, core 8 and core 4 have $\nabla V = 17.2 \text{ km s}^{-1} \text{ pc}^{-1}$ and $\nabla V = -11.3 \text{ km s}^{-1} \text{ pc}^{-1}$, respectively. The origin of the observed velocity gradients with different directions are likely to be the local effects such as rotating motions or unresolved multiple components. If the observed velocity fields come from rotations, the rotational energy E_{rot} can be estimated under the assumption of solid-body rotation as (Belloche 2013)

$$E_{\text{rot}} = \frac{1}{2} I \Omega^2 = \frac{1}{2} \left[\frac{2}{3} M R^2 \left(\frac{3 - \alpha}{5 - \alpha} \right) \right] \left(\frac{|\nabla V|}{\sin i} \right)^2 \quad (7)$$

where i is the inclination angle of the rotational axis to the line of sight, and α indicates a power-law density profile of $\rho \propto r^{-\alpha}$. The gravitational energy can also be derived as

$$E_{\text{grav}} = -\frac{GM^2}{R} \left(\frac{3 - \alpha}{5 - 2\alpha} \right). \quad (8)$$

To estimate the ratio of rotational to gravitational energy (β_{rot}) for these cores, we assume a uniform density profile, i.e., $\alpha = 0$, and a random-averaged inclination angle of $\langle \sin i \rangle = \pi/4$. It turns out that core 8 has β_{rot} ranging from 0.04–0.11, and core 4 has β_{rot} ranging from 0.02–0.06. This means that rotations of these cores are significant but not dominant in the energetics.

4.4.2. Major-axis Analysis

The velocity fields along the major axes of the filaments are also analyzed. Using the central velocity (V_{LSR}) and the peak intensity determined from the hyperfine spectral fitting (see Section 4.2), we plot the intensity and velocity variations along the filament major axis in Figure 9, where the horizontal axes represent the offset (from north to south) in arcseconds, and the

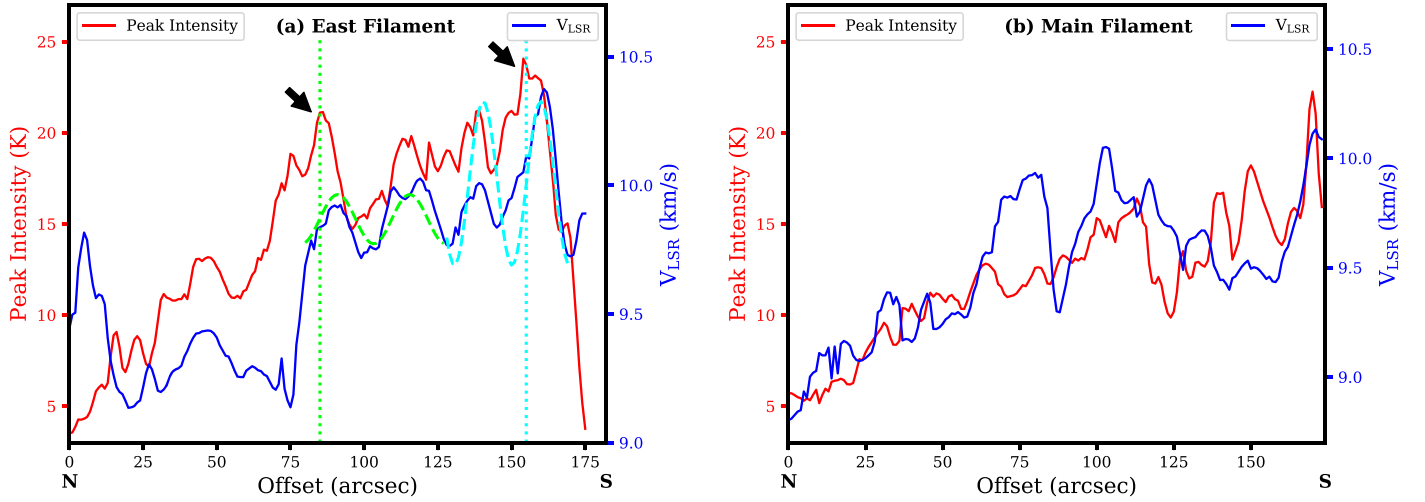


Figure 9. Comparison between the intensity and velocity variations along the major axis of the (a) east filament and the (b) main filament. In the left panel, the arrows indicate two intensity peaks which correspond to core 8 and 4, showing positional shifts relative to their velocity peaks; the dashed curves are sinusoidal fits to the velocity variation, and the two vertical lines show the locations shifted by $\lambda/4$ from the fitted sinusoidal peaks of core 8 and 4. Offset 0 is at the northernmost position of the filament, i.e., (R.A., decl.) = ($5^{\text{h}}35^{\text{m}}19^{\text{s}}.4$, $-5^{\circ}19'29''.43$) for the east filament and ($5^{\text{h}}35^{\text{m}}20^{\text{s}}.4$, $-5^{\circ}17'50''.43$) for the main filament.

vertical axes show the peak intensity on the left and the V_{LSR} on the right.

Analysis of the east filament (see Figure 9(a)) reveals the oscillations in both intensity and velocity. It is found that there are positional shifts between the intensity and velocity peaks toward cores 8 and 4. This is similar to the feature observed in two of the filaments in L1517 (Hacar & Tafalla 2011). The velocity oscillation along the filament can be related to the core-forming motions. If the gas flow is converging to the center of the core, its velocity with respect to the one at the core center is positive in one side and negative in the other side of the density peak. According to the kinematic model proposed in Hacar & Tafalla (2011), where sinusoidal perturbations were assumed for both density and velocity, a $\lambda/4$ phase shift between the two distributions is predicted. In Figure 9(a), we show the sinusoidal fits to the velocity oscillation in the east filament. In addition, the locations of the intensity peaks toward cores 8 and 4 match well with the $\lambda/4$ shift from the two corresponding sinusoidal peaks.

Figure 9(b) shows the intensity and velocity plot for the main filament. Although there is a secondary velocity component toward part of this filament, the velocities determined from the fitting represent the ones of the major component. In the main filament, the relations between the intensity and velocity variations are unclear. This is probably because of the evolutionary stage of the main filament. Previous 1.3 mm observations with the SMA (Teixeira et al. 2016) revealed CO molecular outflows associated with some cores in the main filament, including core 5. It is therefore likely that some of the cores in the main filament have already harbor young protostars in the Class 0 stage.

In contrast, no evidence of protostars have been observed in the east filament, and the positional shift between its intensity and velocity peaks may indicate that core formation is still ongoing in the east filament. As the evolutionary stage of different filaments can vary (Myers 2017), it is possible that the east filament is in an earlier evolutionary phase than the main filament with star formation signature.

5. Discussion

5.1. Filament and Core Properties

As shown in Table 1, all three filaments with core fragmentation have line masses $\gtrsim 80 M_{\odot} \text{ pc}^{-1}$. In contrast, the filaments with lower line masses such as filaments 3, 4, and 9 do not contain cores. However, three filaments having the line masses close to $80 M_{\odot} \text{ pc}^{-1}$ (filaments 1, 2, and 5) and filament 6 with the largest line mass do not contain any cores. Therefore, although line masses are often used as an indicator of the star formation stage of a filament (Heitsch 2013; Palmeirim et al. 2013; Li et al. 2014), it may not be a conclusive discriminator, which is also stated in Dhabal et al. (2018).

To investigate the internal dynamics of the filaments, we derive the nonthermal velocity dispersion (Δv_{nt}) by using the equation

$$\Delta v_{\text{nt}} = \sqrt{\frac{(\Delta v)^2}{8 \ln 2} - \frac{k \cdot T_{\text{kin}}}{\mu (N_2 H^+)}} \quad (9)$$

where Δv is the line width in FWHM obtained from the hyperfine fitting, and μ is the molecular mass. The nonthermal velocity dispersion can be compared with the thermal sound speed

$$c_s(T) = \sqrt{\frac{k \cdot T_{\text{kin}}}{\mu (H_2)}}. \quad (10)$$

Then, the critical line mass for an infinite filament in hydrostatic equilibrium can be calculated as (Stodolkiewicz 1963; Ostriker 1964)

$$M_{\text{crit}} = \frac{2(\Delta v_{\text{eff}})^2}{G} = \frac{2}{G} [c_s(T)^2 + (\Delta v_{\text{nt}})^2] \quad (11)$$

where Δv_{eff} is defined as the effective velocity dispersion considering both thermal and nonthermal effects.

Based on the non-LTE results in Section 4.3, we take $T_{\text{kin}} = 20 \text{ K}$ for estimation, which leads to $c_s(T) = 0.287 \text{ km s}^{-1}$. In the case of the purely thermally-supported filament,

$M_{\text{crit}} = 38.4 M_{\odot} \text{pc}^{-1}$. Due to the rather large nonthermal velocity dispersion, the critical line masses listed in the OMC1 filaments are $\sim 2\text{--}4$ times larger than the purely thermally-supported case. Table 1 reveals that 7 of the 11 filaments have $0.5 \leq M_{\text{lin}}/M_{\text{crit}} \leq 1.5$, suggesting that most of the filaments are gravitationally bound. Filaments 3, 4, and 9 having low line masses are found to have $M_{\text{lin}}/M_{\text{crit}} < 0.5$ and thus may be gravitationally unbound. On the other hand, filament 8 has $M_{\text{lin}}/M_{\text{crit}} < 0.5$ even though this filament contains cores. This filament resides in OMC1-South, where a cluster of young stellar objects (YSOs) have already been formed (Zapata et al. 2004, 2006). Due to the powerful outflows from these YSOs, the gas in this region is highly turbulent. Thus, filament 8 has the largest line width of $\sim 3 \text{ km s}^{-1}$ among all the filaments, leading to a high M_{crit} and a low $M_{\text{lin}}/M_{\text{crit}}$ ratio. The low $M_{\text{lin}}/M_{\text{crit}}$ value could imply that filament 8 is in the phase of disruption. Another possibility is the high external pressure in this region. If the filament is confined by external pressure, the filament is prone to fragmentation even though its line mass is smaller than the critical line mass (e.g., Fischera & Martin 2012). Since filament 8 in OMC1-South is adjacent to the Orion Nebula Cluster, the high external pressure from hot and diffuse gas in the cluster could lead the core formation in this filament.

Our results show that the filaments in OMC1 have $M_{\text{lin}}/M_{\text{crit}} < 1.5$, which is consistent with that of Hacar et al. (2018) based on their N_2H^+ 1–0 data. However, even though the derived $M_{\text{lin}}/M_{\text{crit}}$ ratios are similar, both the M_{lin} and M_{crit} determined from our data are higher than those of Hacar et al. (2018) by a factor of a few. While they used N_2H^+ intensities to estimate column densities of H_2 , we use the volume densities of H_2 derived from the non-LTE analysis. The empirical relation between N_2H^+ intensities to H_2 column densities used by Hacar et al. (2018) has large scatter. The inclination of each filament is also uncertain. On the other hand, the uncertainty in inclination does not affect our estimation. However, the M_{lin} derived under our assumption of uniform density inside the filaments (excluding the cores) might be overestimated if the filaments have radial density profiles. The difference in M_{crit} likely results from the difference between the line widths observed in N_2H^+ 3–2 ($\sim 1.0 \text{ km s}^{-1}$) and 1–0. This is partly because of the difference in the beam size of our measurement ($5''.4$) and that of Hacar et al. (2018) ($4''.5$); the spectra observed with the larger beam contain the nonthermal motion in the larger area. The hyperfine components of 3–2, which are much more complicated than those of 1–0, introduce additional uncertainty in the derived line width if the relative intensities of the hyperfine components are different from the LTE values.

Table 2 shows that most of the cores have masses (M_{core}) ranging from $1\text{--}10 M_{\odot}$. Both the sizes and the masses of these cores are larger than those determined by Teixeira et al. (2016), because multiple smaller-scale cores were revealed in their 1.3 mm continuum data using the SMA. These masses can also be compared with the masses inferred by the virial theorem. By assuming a uniform density in the cores, the virial mass (M_{vir}) can be derived as

$$M_{\text{vir}} = \frac{5 R_{\text{eff}} (\Delta v)^2}{8 G \ln 2}, \quad (12)$$

where R_{eff} is an effective radius of the core, and Δv is a typical line width. The line width Δv was determined from the

hyperfine fitting except for cores 6, 7, and 9 having multiple velocity components along the line of sight.

As shown in Table 2, the measured core masses are similar to the calculated virial masses, indicating that most of the cores are gravitationally bound. One of the cores, core 5, already shows the signatures of star formation; toward this core, there is an infrared source and a clear bipolar outflow in CO (Teixeira et al. 2016). The velocity dispersion as well as M_{vir} is large in the southern cores i.e., cores 1 and 2, because of the strong turbulence from the stellar activities in OMC1-South (Zapata et al. 2006; Palau et al. 2018).

5.2. External Heating from High-mass Stars

The N_2H^+ 3–2/1–0 ratio map presented in Figure 3 shows higher ratios in the eastern part of OMC1. From the non-LTE model shown in Figure 7, regions with a higher intensity ratio generally indicate a higher kinetic temperature. This suggests that the eastern OMC1 has higher temperatures compared with the remaining area.

We find that the overall distribution of the high-ratio gas is similar to that of the CN and C_2H molecules presented in Ungerechts et al. (1997) and Melnick et al. (2011). Since CN and C_2H are sensitive to the presence of UV radiation (Fuente et al. 1993; Stauber et al. 2004), it is likely that the higher temperatures in the eastern OMC1 are caused by the UV heating from the high-mass stars in M42. For example, UV photons from the θ^1 Ori C at (R.A., decl.) = ($5^{\text{h}}35^{\text{m}}16^{\text{s}}.5$, $-5^{\circ}23'22''.8$), which is southeast of the Orion KL, could be one of the major heating sources. In addition, the [C I]/CO intensity ratio map in Shimajiri et al. (2013) shows a ratio peak of ~ 0.17 around the position (R.A., decl.) = ($5^{\text{h}}35^{\text{m}}20^{\text{s}}$, $-5^{\circ}18'30''$), implying that UV radiation also contributes to the heating of this region. Possible heating sources include the exciting star of M43—NU Ori at (R.A., decl.) = ($5^{\text{h}}35^{\text{m}}31^{\text{s}}.0$, $-5^{\circ}16'12''$), which is northeast of the OMC1 region.

The external heating scenario also explains the 3–2/1–0 ratios inside and outside the filaments. As shown in Figure 3, heating features are seen only outside the filament regions, while temperatures inside the filaments remain significantly lower. Wiseman & Ho (1998) reported the variation of NH_3 (J, K) = (2, 2) to (1, 1) line intensity ratio in the filaments; the higher ratio (i.e., higher temperature) gas appears between the emission peaks with a lower ratio (i.e., lower temperature). Such a patchy heating pattern in the filaments does not appear in the N_2H^+ . There is no significant difference in the N_2H^+ 3–2/1–0 ratio between the core regions and the low-intensity regions in the filaments. This is probably because the N_2H^+ lines have higher critical densities than the NH_3 trace in the inner and denser part of the filaments where the gas is well shielded from the external radiation.

Apart from external UV heating, local heating from Orion KL has been discussed on the basis of previous observations (Wiseman & Ho 1998; Zapata et al. 2011; Bally et al. 2017; Tang et al. 2018). However, since N_2H^+ emission is missing toward Orion KL, local heating around the KL core ($\sim 100 \text{ K}$) is not observed in our data. The 3–2/1–0 ratio at the position of core 4, ~ 2.0 , is significantly higher than other regions of the east filament. This could be the effect of the local heating from Orion KL.

5.3. Global Collapse of OMC1

Recent studies have shown that large-scale dynamical collapse is important in high-mass star-forming regions (e.g., Hartmann & Burkert 2007; Hacar et al. 2017). The snapshots from the magnetohydrodynamic (MHD) simulation of globally collapsing clouds presented in Schneider et al. (2010) and Peretto et al. (2013) reveal multiple filaments and sharp boundaries of radial velocity changes that separate the cloud into several regions, and these regions and filaments converge toward the massive core at the center. The radial velocity distribution of OMC1 shows the trimodal pattern centered near Orion KL with the sharp boundaries between the northern and western regions (Figure 6(a)) and the northern and southern regions (Figure 6(b)). In addition, the radial velocities in the western region monotonically decrease from north to south, and continue to the velocity gradient in the southern region (Figure 6(b)). This velocity gradient corresponds to the part of the V-shaped velocity structure centered around the OMC1-South, which is interpreted as the presence of accelerated gas motion inflowing toward the Orion Nebula Cluster (Hacar et al. 2017). Our results have revealed that the gas in the western and southern regions contributes to this inflow.

Such a global collapse picture is also supported by the morphology of the magnetic field in OMC1. The magnetic field in OMC1 revealed by the B-fields in Star-forming Region Observations survey using the James Clerk Maxwell Telescope shows a well-ordered U-shaped structure, which can be explained by the distortion of an initially cylindrically symmetric magnetic field due to large-scale gravitational collapse (Pattle et al. 2017). Interestingly, the filaments in the northern and southern regions are almost perpendicular to the local magnetic field direction, while those in the western region such as filaments 3, 4, and 5 are aligned along the magnetic field. This implies that the filaments in the western region are feeding material along the magnetic field lines to the Orion Nebula Cluster, as predicted from the MHD simulation of global collapse (Schneider et al. 2010).

6. Conclusion

We conducted N_2H^+ 3–2 line observations toward the OMC1 region using the SMA and SMT. The SMA data are combined with the SMT data in order to recover the spatially extended emission. The filaments and cores in OMC1 have been identified, and their physical properties are derived. Using the N_2H^+ 1–0 data provided by Hacar et al. (2018), we conducted non-LTE analysis, and determined the kinetic temperatures and H_2 densities of the filaments and cores. We also examine the gas kinematics inside the two prominent (main and east) filaments and compare them with the filament/core formation models. The main results are summarized as the following:

1. The combined SMA and SMT image in N_2H^+ 3–2 reveals multiple filamentary structures having typical widths of 0.02–0.03 pc. In total, 11 filaments and 10 cores are identified. Cores are found in three filaments with line masses $\gtrsim 80 M_\odot \text{ pc}^{-1}$. The masses of the cores are in the range of 1–10 M_\odot except the most massive one with $>14 M_\odot$ in OMC1-South. Up to $\sim 65\%$ of the filaments are gravitationally bound, which could be current or future sites for star formation.
2. The result of non-LTE analysis shows that the kinetic temperature is enhanced in the eastern part of OMC1. This is probably because of the external heating from high-mass stars in M42 and M43 (e.g., θ^1 Ori C and NU Ori). It is found that the filament regions with higher densities of $n_{\text{H}_2} \sim 10^7 \text{ cm}^{-3}$ have lower temperatures ($T_{\text{kin}} \sim 15\text{--}20 \text{ K}$) than their surrounding regions. The lower temperatures in the filaments can be explained by the shielding from the external heating by dense gas.
3. The moment 1 image reveals that OMC1 consists of three subregions with different radial velocities divided by the sharp velocity transitions. Three subregions intersect with each other at the location of Orion KL. The radial velocities in the western region monotonically decrease from north to south, and continue this trend in the southern region. The observed velocity structure suggests the presence of global gas flow toward the Orion Nebula Cluster. Such a global collapse is also supported by the observed morphology of magnetic fields and large-scale gas kinematics in the integral-shaped filament.
4. Nonthermal motion plays an important role in the OMC1 filaments. There is no systematic velocity gradient along the minor axes of the OMC1 filaments. Although the velocity gradient of $\sim 0.3 \text{ km s}^{-1}$ is observed in the east filament, the direction of the velocity gradient is different at different locations.
5. Two cores in the east filament show positional shifts between their intensity and velocity peaks along the filament major axis. It is possible that core formation is still ongoing in this filament. On the other hand, there is no such positional shift in the main filament. It is therefore likely that the east filament is in an earlier evolutionary phase than the main filament, which shows the signatures of star formation.

We thank the staff of the SMA and the SMT for the operation of our observations and their support in data reduction. We thank Dr T.-H. Hsieh for helping us with the SMT observations. The SMA is a joint project between the Smithsonian Astrophysical Observatory and the Academia Sinica Institute of Astronomy and Astrophysics and is funded by the Smithsonian Institution and the Academia Sinica. N.H. acknowledges a grant from the Ministry of Science and Technology (MoST) of Taiwan (MoST 108-2112-M-001-017).

Facilities: SMA, SMT.

Software: MIR/IDL (<https://www.cfa.harvard.edu/rtcd/SMAdata/process/mir/>), MIRIAD (Sault et al. 1995), GILDAS/CLASS (<http://www.iram.fr/IRAMFR/GILDAS>), Fil-Finder (Koch & Rosolowsky 2015), Clumpfind (Williams et al. 1994).

ORCID iDs

Yu-Hsuan Teng  <https://orcid.org/0000-0003-4209-1599>
Naomi Hirano  <https://orcid.org/0000-0001-9304-7884>

References

- André, P., Di Francesco, J., Ward-Thompson, D., et al. 2014, in *Protostars and Planets VI*, ed. H. Beuther et al. (Tucson, AZ: Univ. Arizona Press), 27
Bally, J., Ginsburg, A., Arce, H., et al. 2017, *ApJ*, 837, 60
Bally, J., Langer, W. D., Stark, A. A., & Wilson, R. W. 1987, *ApJL*, 312, L45

- Belloche, A. 2013, in EAS Publ. Ser. 62, Role and Mechanisms of Angular Momentum Transport During the Formation and Early Evolution of Stars, ed. P. Hennebelle & C. Charbonnel (Les Ulis: EDP Sciences), 25
- Beuther, H., Ragan, S. E., Johnston, K., et al. 2015, *A&A*, 584, A67
- Caselli, P., Walmsley, C. M., Zucconi, A., et al. 2002, *ApJ*, 565, 331
- Dhabal, A., Mundy, L. G., Rizzo, M. J., Strom, S., & Teuben, P. 2018, *ApJ*, 853, 169
- Fischera, J., & Martin, P. G. 2012, *A&A*, 542, A77
- Fuente, A., Martin-Pintado, J., Cernicharo, J., & Bachiller, R. 1993, *A&A*, 276, 473
- Hacar, A. 2018, ORION-4D: Integral Shape Filament ALMA+IRAM30m N2H+(1-0) datacube, V1, Harvard Dataverse, doi:10.7910/DVN/DBZUOP
- Hacar, A., Alves, J., Tafalla, M., & Goicoechea, J. R. 2017, *A&A*, 602, L2
- Hacar, A., & Tafalla, M. 2011, *A&A*, 533, A34
- Hacar, A., Tafalla, M., Forbrich, J., et al. 2018, *A&A*, 610, A77
- Hartmann, L., & Burkert, A. 2007, *ApJ*, 654, 988
- Heitsch, F. 2013, *ApJ*, 769, 115
- Koch, E. W., & Rosolowsky, E. W. 2015, *MNRAS*, 452, 3435
- Li, D. L., Esimbek, J., Zhou, J. J., et al. 2014, *A&A*, 567, A10
- Melnick, G. J., Tolls, V., Snell, R. L., et al. 2011, *ApJ*, 727, 13
- Menten, K. M., Reid, M. J., Forbrich, J., & Brunthaler, A. 2007, *A&A*, 474, 515
- Monsch, K., Pineda, J. E., Liu, H. B., et al. 2018, *ApJ*, 861, 77
- Myers, P. C. 2009, *ApJ*, 700, 1609
- Myers, P. C. 2017, *ApJ*, 838, 10
- Olmi, L., & Testi, L. 2002, *A&A*, 392, 1053
- Ostriker, J. 1964, *ApJ*, 140, 1056
- Palau, A., Zapata, L. A., Román-Zúñiga, C. G., et al. 2018, *ApJ*, 855, 24
- Palmeirim, P., Andre, Ph., Kirk, J., et al. 2013, *A&A*, 550, A38
- Pattle, K., Ward-Thompson, D., Berry, D., et al. 2017, *ApJ*, 846, 122
- Peretto, N., Fuller, G. A., Duarte-Cabral, A., et al. 2013, *A&A*, 555, A112
- Sault, R. J., Teuben, P. J., & Wright, M. C. H. 1995, in ASP Conf. Ser. 77, Astronomical Data Analysis Software and Systems IV, ed. R. A. Shaw, H. E. Payne, & J. J. E. Hayes (San Francisco, CA: ASP), 433
- Schneider, N., Csengeri, T., Bontemps, S., et al. 2010, *A&A*, 520, A49
- Schneider, S., & Elmegreen, B. G. 1979, *ApJS*, 41, 87
- Shimajiri, Y., Sakai, T., Tsukagoshi, T., et al. 2013, *ApJL*, 774, L20
- Stauber, P., Doty, S. D., van Dishoeck, E. F., et al. 2004, *A&A*, 425, 577
- Stodolkiewicz, J. S. 1963, *AcA*, 13, 30
- Tang, X. D., Henkel, C., Menten, K. M., et al. 2018, *A&A*, 609, A16
- Teixeira, P. S., Takahashi, S., Zapata, L. A., & Ho, P. T. P. 2016, *A&A*, 587, A47
- Ungerechts, H., Bergin, E. A., Goldsmith, P. F., et al. 1997, *ApJ*, 482, 245
- Van der Tak, F. F. S., Black, J. H., Schoier, F. L., et al. 2007, *A&A*, 468, 627
- Williams, J. P., de Geus, E. J., & Blitz, L. 1994, *ApJ*, 428, 693
- Wiseman, J., & Ho, P. T. P. 1998, *ApJ*, 502, 676
- Zapata, L. A., Ho, P. T. P., Rodríguez, L. F., et al. 2006, *ApJ*, 653, 398
- Zapata, L. A., Rodríguez, L. F., Kurtz, S. E., et al. 2004, *ApJL*, 610, L121
- Zapata, L. A., Schmid-Burgk, J., & Menten, K. M. 2011, *A&A*, 529, A24